Loss of PTPMT1 limits mitochondrial utilization of carbohydrates and leads to muscle atrophy and heart failure in tissue-specific knockout mice

Hong Zheng[1, 2, 8], Qianjin Li[1, 8], Shanhu Li[1, 2, 8], Zhiguo Li[1], Marco Brotto[3], Daiana Weiss[4], Domenick Prosdocimo[5], Chunhui Xu[1], Ashruth Reddy[1], Michelle Puchowicz[6], Xinyang Zhao[7], M. Neale Weitzmann[4], Mukesh K. Jain[5], and Cheng-Kui Qu[1, 2, *]

[1] Department of Pediatrics, Children Healthcare of Atlanta, Emory University School of Medicine, Atlanta, GA 30322. [2] Department of Medicine, Case Western Reserve University, Cleveland, OH 44106. [3] College of Nursing & Health Innovation, University of Texas-Arlington, Arlington, TX 76019. [4] Department of Medicine, Emory University School of Medicine, Atlanta, GA 30322; Atlanta Department of Veterans Affairs Medical Center, Decatur, GA 30033. [5] Case Cardiovascular Research Institute, Department of Medicine, Case Western Reserve University, Cleveland, OH 44106. [6] Case Mouse Metabolic Phenotyping Center, Case Western Reserve University, Cleveland, OH 44106. [7] Department of Biochemistry and Molecular Genetics, University of Alabama at Birmingham, Birmingham, AL 35294.

[8] These authors contributed equally to this work.

Keywords: PTPMT; Mitochondria; Bioenergetics; Heart; Skeletal muscle.

Conflict of interests: The authors have declared that no conflict of interest exists.

* Corresponding author:
CK Qu, M.D., Ph.D.
Department of Pediatrics
Emory University School of Medicine
1760 Haygood Drive NE, HSRB E302
Atlanta, GA 30322

Tel: 404-727-5037
Fax: 404-727-4455
Email: cheng-kui.qu@emory.edu

ABSTRACT

While mitochondria in different tissues have distinct preferences for energy sources, they are flexible in utilizing competing substrates for metabolism according to physiological and nutritional circumstances. However, the regulatory mechanisms and significance of metabolic flexibility are not completely understood. Here we report that the deletion of *PTPMT1,* a mitochondria-based phosphatase, critically alters mitochondrial fuel selection – the utilization of pyruvate, a key mitochondrial substrate derived from glucose (the major simple carbohydrate), is inhibited, whereas the fatty acid utilization is enhanced. *PTPMT1* knockout does not impact the development of the skeletal muscle or heart. However, the metabolic inflexibility ultimately leads to muscular atrophy, heart failure, and sudden death. Mechanistic analyses reveal that the prolonged substrate shift from carbohydrates to lipids causes oxidative stress and mitochondrial destruction, which in turn results in marked accumulation of lipids and profound damage in the knockout muscle cells and cardiomyocytes. Interestingly, *PTPMT1* deletion from the liver or adipose tissue does not generate any local or systemic defects. These findings suggest that PTPMT1 plays an important role in maintaining mitochondrial flexibility and that their balanced utilization of carbohydrates and lipids is essential for both the skeletal muscle and the heart despite the two tissues having different preferred energy sources.

INTRODUCTION

Mitochondria, the powerhouse of the cell, produce energy in the form of ATP from the breakdown of carbohydrates, fats, and proteins. Mitochondrial abundance and their preferences for metabolic substrates differ in various cell types [1]. While mitochondria are abundant in red skeletal muscles such as Soleus, and the heart, the mitochondrial content in white muscles, such as Extensor Digitorum Longus (EDL), is much lower. Mitochondria in the skeletal muscle and heart have distinct preferences for energy sources - skeletal muscle mitochondria prefer glucose (the major simple carbohydrate) as the substrate, whereas cardiac mitochondria mainly use fatty acids as the fuel. Moreover, different types of skeletal muscle cells (fibers) utilize glucose to produce energy in different mechanisms - in slow-twitch oxidative muscle fibers glucose (via pyruvate, a critical metabolite derived from glucose) is predominantly oxidized within the mitochondria to generate energy, whereas in fast-twitch muscle fibers pyruvate is primarily reduced to lactate in the cytosol promoting glycolytic flux to rapidly produce energy and support quick contractions. Nevertheless, both muscle and heart mitochondria are flexible in selecting substrates in response to stress (exercise, fasting, etc.) and under disease conditions (heart failure, diabetes, etc.) [2-5]. It remains to be determined how mitochondrial utilization of various competing metabolic substrates is coordinated and whether disruption of mitochondrial flexibility in fuel selection affects the function of the heart and skeletal muscle.

PTPMT1, encoded by nuclear DNA, is localized to the mitochondrion and anchored at the inner membrane [6]. It dephosphorylates phosphatidylinositol phosphates (PIPs). PIPs are a class of membrane phospholipids that bind to a distinctive set of effector proteins, thereby regulating a characteristic suite of cellular processes, including membrane trafficking and ion channel/transporter functions [7,8]. PTPMT1 is

also involved in the synthesis of cardiolipin by converting phosphotidylglecerol phosphate to phosphotidylglecerol, the precursor of cardiolipin [9]. Global knockout of *PTPMT1* results in developmental arrest and post-implantation lethality [9,10]. Our previous studies suggest that PTPMT1 facilitates mitochondrial metabolism largely by dephosphorylation of downstream PIP substrates [11-13] that appear to inhibit mitochondrial oxidative phosphorylation but enhance cytosolic glycolysis by activation of mitochondrial uncoupling protein 2 (UCP2) [11], a transporter of four-carbon (C4) dicarboxylate intermediates of the tricarboxylic acid (TCA) cycle that has been shown to regulate cellular energetics by limiting mitochondrial oxidation of glucose [14-18]. *PTPMT1* is highly expressed in the heart and skeletal muscle [10]. In the present study, we exploit *PTPMT1* tissue-specific knockout models to address the role and mechanisms of PTPMT1-facilitated mitochondrial metabolism in these tissues. We find that PTPMT1 plays an important role in facilitating mitochondrial utilization of carbohydrates and that balanced fuel selection is essential for maintaining both muscle and heart functions despite the two tissues having distinct preferences for energy sources.

RESULTS

Knockout of *PTPMT1* from skeletal muscles results in defective contractile function and progressive muscle atrophy

To determine the role of PTPMT1-mediated metabolism in the skeletal muscle and heart, we generated tissue-specific *PTPMT1* knockout mice (*PTPMT1*$^{fl/fl}$/*CKMM-Cre*$^{+}$) by crossing *PTPMT1 floxed* mice [11] and muscle creatine kinase promoter-driven *Cre* transgenic mice (*CKMM-Cre*), which express the Cre recombinase in the skeletal muscle and heart starting at embryonic day 13 [19]. Quantitative reverse transcription PCR (qRT-PCR) showed ~95% and ~80% deletion of *PTPMT1* in the skeletal muscle and

heart in *PTPMT1*$^{fl/fl}$/*CKMM-Cre*$^{+}$ mice, respectively (Figure 1A). These animals were indistinguishable from their wild-type (WT, *PTPMT1*$^{+/+}$/*CKMM-Cre*$^{+}$) littermates up to 3 months of age, suggesting that *PTPMT1* deletion did not affect muscle or heart development. The knockout mice exhibited reduced weight gain starting at 4 to 5 months and their body sizes were significantly smaller than those of control mice at 8 months (Figure 1A). Muscle wasting was observed in *PTPMT1*$^{fl/fl}$/*CKMM-Cre*$^{+}$ mice at 8 months or older (Figure 1A). Histopathological examination of skeletal muscles of these knockout mice revealed characteristic changes of muscle atrophy - marked variations in muscle fiber diameters and the presence of ghost fibers or more interstitial space (Figure 1B). In addition, Masson's trichrome staining revealed increased collagen-rich fibrotic regions in *PTPMT1* knockout muscles (Figure 1B). We then examined *PTPMT1* knockout mice at 6-8 months (prior to the onset of muscle wasting). *PTPMT1*$^{fl/fl}$/*CKMM-Cre*$^{+}$ mice became fatigued faster and fell more quickly than *PTPMT1*$^{+/+}$/*CKMM-Cre*$^{+}$ control animals in wire hang tests, indicating muscle weakness (Figure 1C). In treadmill exercise tests, both male and female knockout mice displayed reduced maximum speed (Figure 1D), endurance (Figure 1E), and distance of the run (Supplemental Figure 1A). To determine whether the reduced muscle strengths of the knockout mice resulted from muscle cell-intrinsic defects, isometric contractile properties of isolated muscles were examined. *Ex vivo* force-frequency measurements were performed on Soleus, a more oxidative muscle with a higher percentage of slow-twitch Type I fibers, and EDL, a more glycolytic muscle with a higher percentage of fast-twitch Type II fibers. Both knockout Soleus and EDL showed decreased optimal length, the length of the muscle at which maximal force was achieved (Supplemental Figure 1, C and D). Specific force production of *PTPMT1* knockout Soleus (Supplemental Figure 1E) and EDL (Supplemental Figure 1E) was decreased. However, normalized force production was decreased only in knockout Soleus (Figure 1F), but not in knockout EDL (Figure 1G). These data suggest that

PTPMT1 plays a more important role in oxidative than glycolytic muscle fibers although both knockout Soleus and EDL developed muscle atrophy subsequently.

To determine the impact of PTPMT1 depletion from the skeletal muscle and heart on the metabolism of the whole body, we measured plasma glucose and fatty acid levels and found that they were comparable in *PTPMT1*$^{fl/fl}$/*CKMM-Cre*$^{+}$ and *PTPMT1*$^{+/+}$/*CKMM-Cre*$^{+}$ mice (Supplemental Figure 2A). Plasma levels of lactate (Supplemental Figure 2B) and lipid metabolic products (Supplemental Figure 2C) in *PTPMT1* knockout mice were also relatively normal (except that cholesterol and nonesterified fatty acids levels were decreased and marginally increased, respectively, in female knockout mice). Adipokine array assays of the plasma showed no or subtle differences in Adiponectin, Leptin, Lipocalin-2, ANGPTL3, Resistin, FGF-21, DPPIV, Fetuin A, IGF-1, etc. between *PTPMT1* knockout and control mice (Supplemental Figure 2D). In addition, no differences in glucose tolerance tests were observed between *PTPMT1* knockout and control mice (Supplemental Figure 2E). Furthermore, we assessed the expression levels of key enzymes involved in glucose and lipid metabolism in *PTPMT1* knockout muscles. No changes in HK2, PKM1, LDHA, DICER1, MCAD (ACADM), ACADL, HADHA, CPT2, or FABP3 were found. However, the expression of CPT1B, was increased in *PTPMT1* knockout muscles (Supplemental Figure 2, F and G). These results suggest that systemic glucose and lipid metabolism in these tissue-specific knockout mice was not significantly changed, but fatty acid partitioning for oxidation in the mitochondria was elevated in *PTPMT1* knockout muscles.

PTPMT1 depletion ultimately leads to mitochondrial damage and bioenergetic stress in knockout skeletal muscles

Gömöri trichrome staining revealed ragged red fibers in *PTPMT1* knockout skeletal muscles (Figure 2A), as observed in various types of human mitochondrial myopathies. Electron microscopic analyses showed that interfibrillar mitochondria in knockout Soleus and EDL were disorganized and enlarged, in contrast to normal mitochondria that typically reside in pairs and position on either side of the Z-disc in control muscles. In addition, there was a massive accumulation of subsarcolemmal mitochondria in the knockout muscles, whereas the content of intermyofibrillar mitochondria decreased (Figure 2B). Although EDL, unlike Soleus, uses more cytosolic glycolysis than mitochondrial oxidative phosphorylation for energy production, the mitochondrial structural changes appeared to be more severe in EDL than Soleus in the knockout mice (Figure 2B). Furthermore, a massive accumulation of intramyofibrillar lipids were detected by Oil Red O staining in 6-month or older *PTPMT1* knockout muscles (Figure 2C).

Total mitochondrial content in *PTPMT1* knockout Soleus and EDL also slightly decreased compared to that in control muscles (Figure 2D). ATP levels in both knockout Soleus and EDL decreased significantly compared to WT counterparts (Figure 2E). Consistent with these data, the energetic stress sensor, AMP-activated kinase (AMPK), was highly activated in *PTPMT1*$^{fl/fl}$/*CKMM-Cre*$^{+}$ muscles as determined by the phosphorylation levels of Thr^{172} (Figure 2F). Acetyl-CoA carboxylase (ACC), a negative regulator of fatty acid oxidation, was inhibited, as evidenced by a marked increase in the inhibitory phosphorylation of this enzyme (Figure 2F), implying increased fatty acid oxidation in PTPMT1-depleted mitochondria. In agreement with previous findings that AMPK negatively regulates mTOR signaling [20,21], mTOR was substantially inhibited. Activities of S6K, S6, and 4E-BP1, key downstream components of mTOR signaling, were also concomitantly decreased (Figure 2F), indicating diminished anabolic activities and consistent with the muscle atrophy phenotype. Interestingly, Akt activities, as reflected by its

phosphorylation levels (Ser^{473} and Thr^{308}), were increased in *PTPMT1* knockout skeletal muscles, recapitulating mTOR and raptor (a component of the mTOR complex 1) knockout muscles [22,23]. Likely due to the cross-talk between Akt and Ras signaling pathways, Erk activities were also slightly increased in these knockout muscles (Figure 2F).

Given that muscle atrophy developed in *PTPMT1*$^{fl/fl}$/*CKMM-Cre*$^{+}$ mice after 6-8 months, to assess the direct impact of *PTPMT1* deletion on mitochondrial metabolism, it is important to examine mitochondria in young *PTPMT1* knockout mice before the tissue damage. Expression levels of electron transport chain complexes in these PTPMT1-ablated mitochondria were not changed (Supplemental Figure 3A). Total cellular ATP levels in *PTPMT1* knockout muscles at this age were comparable to those in control tissues (Supplemental Figure 3B), and the knockout muscles did not show bioenergetic/metabolic stress (Supplemental Figure 3C). We also checked LC3-I/II levels in *PTPMT1* knockout muscles and found no evidence of elevated autophagic activities (Supplemental Figure 3D). These results indicate that the decrease in total cellular ATP levels in older knockout muscles (Figure 2E) was a secondary not direct effect of PTPMT1 depletion.

PTPMT1 loss impairs mitochondrial utilization of pyruvate, whereas the fatty acid utilization is enhanced

We next sought to address the mechanisms by which PTPMT1 loss impacts mitochondrial metabolism. To avoid secondary effects, we examined mitochondrial metabolic activities of *PTPMT1* knockout muscles in 3-month-old *PTPMT1*$^{fl/fl}$/*CKMM-Cre*$^{+}$ and *PTPMT1*$^{+/+}$/*CKMM-Cre*$^{+}$ mice. Knockout muscle tissues showed decreased maximal reserve oxidative capacities in the presence of full substrates (Figure

3A), consistent with our previous observations from other *PTPMT1* knockout cell types [11,12,24]. In addition, we isolated mitochondria from young skeletal muscles and assessed mitochondrial metabolism in the presence of ADP and a single metabolic substrate by real-time measurement of ATP synthesis-driven oxygen consumption. When pyruvate, a critical metabolite derived from glucose, was provided as the sole substrate, ATP synthesis-driven oxygen consumption in PTPMT1-deficient mitochondria was markedly decreased (Figure 3B), suggesting that mitochondrial utilization of pyruvate was diminished in the absence of PTPMT1. Interestingly, we observed enhanced oxygen consumption in these mitochondria when fatty acids were supplied as the fuel (Figure 3C). A slightly increased respiratory response in PTPMT1-depleted mitochondria was also detected when glutamate, another mitochondrial substrate, was provided (Figure 3D). Importantly, feeding with succinate, the substrate for Complex II of the electron transport chain, resulted in similar oxygen consumption in PTPMT1 null and control mitochondria (Figure 3E), validating the intact function of the electron transport chain in the knockout mitochondria and excluding flavin adenine dinucleotide and quinone-linked deficiencies. These mechanistic data suggest that PTPMT1 plays an important role in facilitating carbohydrate oxidation in mitochondria.

Consistent with the above notion, intramitochondrial pyruvate levels in the mitochondria freshly isolated from *PTPMT1* knockout muscles decreased by half (Figure 3F). Levels of α-ketoglutarate (α-KG), an important metabolite in the TCA cycle, also decreased in the knockout mitochondria (Figure 3G), although steady-state mitochondrial acetyl-CoA levels were not changed (Figure 3H). To further determine if pyruvate transport efficiency may be reduced in PTPMT1-ablated mitochondria, we incubated fresh mitochondria with pyruvate and measured acute production of α-KG from extramitochondrial pyruvate. As shown in Figure 3I, α-KG production in PTPMT1-ablated mitochondria

was indeed decreased compared to that in control mitochondria. Notably, the activity of pyruvate dehydrogenase (PDH), the enzyme that converts pyruvate to acetyl-CoA to feed the TCA cycle, was not affected in the knockout mitochondria (Figure 3J). These observations together with that the mitochondrial pyruvate carrier/transporter (MPC) was comparably expressed in PTPMT1-ablated mitochondria (Figure 2F) suggest that PTPMT1 null mitochondria were impaired in uptaking pyruvate. Possibly due to an adaptive response to the inhibited pyruvate oxidation in the mitochondria, skeletal muscle fiber-type switching occurred in *PTPMT1*$^{fl/fl}$/*CKMM-Cre*$^{+}$ mice. Muscle fibers in these knockout mice switched from oxidative to glycolytic fibers, as evidenced by a dramatic increase (~170-fold) in the levels of MYH4, a marker of glycolytic fast-twitch Type 2B fibers in *PTPMT1* knockout mice (Figure 3K).

PTPMT1$^{fl/fl}$*/CKMM-Cre*$^{+}$ mice manifest late onset cardiac dysfunction

The heart in *PTPMT1*$^{fl/fl}$/*CKMM-Cre*$^{+}$ mice was less impacted than the skeletal muscle although *PTPMT1* was ~80% deleted from the heart (Figure 1A). At 7 months, when skeletal muscles in these mice displayed atrophy and myocyte damage, no evident histological changes were observed in heart tissues (Supplemental Figure 4A). Echocardiographic examination showed no difference in left ventricle (LV) contractility in *PTPMT1* knockout mice as reflected by similar LV fractional shortening (FS), Ejection Fraction (EF), and the ratio of peak velocity of early to late filling of mitral inflow (E/A) between knockouts and control mice (Supplemental Figure 4B). Mitochondrial content in *PTPMT1*$^{fl/fl}$/*CKMM-Cre*$^{+}$ heart tissues was comparable to that in *PTPMT1*$^{+/+}$/*CKMM-Cre*$^{+}$ control tissues (Supplemental Figure 4C). Total ATP levels in *PTPMT1* knockout heart tissues were marginally but not significantly decreased (Supplemental Figure 4D). Moreover, mitochondria in knockout cardiomyocytes showed

minimal structural changes (Supplemental Figure 4E). Consistent with these observations, no bioenergetic/metabolic stress was detected in the knockout cardiomyocytes according to the activation status of AMPK and mTOR signaling (Supplemental Figure 4F).

However, severe cardiac dysfunction was observed in 10 to 12-month-old *PTPMT1*$^{fl/fl}$/*CKMM-Cre*$^{+}$ mice. Histopathological examination revealed that cardiomyocytes in these animals had uneven sizes and were disorganized (Figure 4A). In addition, fibrotic lesions, indicative of myocardial damage, were observed. Echocardiographic examination showed that LV contractility, as measured by FS and EF in M-mode echocardiographic tracing of LV (Figure 4, B-D) and recorded by M-Mode echocardiography movies (Supplemental Video 1, A and B), was markedly decreased in *PTPMT1* knockout mice. The E/A ratio determined in pulsed-wave Doppler recording of mitral valve inflow was doubled in the *PTPMT1*$^{fl/fl}$/*CKMM-Cre*$^{+}$ heart (Figure 4, E and F). Collectively, these data suggest that PTPMT1 depletion also impaired cardiac function albeit later than skeletal muscle dysfunction.

Heart-specific deletion of *PTPMT1* leads to dilated cardiomyopathy and heart failure

Given that *PTPMT1* was only ~80% deleted from the heart in *PTPMT1*$^{fl/fl}$/*CKMM-Cre*$^{+}$ mice and that impaired skeletal muscle function in these animals may potentially complicate the heart phenotypes, to further investigate the role of PTPMT1-mediated metabolism specifically in cardiac muscles, heart-specific *PTPMT1* knockout mice (*PTPMT1*$^{fl/fl}$/*MYH6-Cre*$^{+}$) were generated by crossing *PTPMT1* conditional mice [11] and *MYH6-Cre* transgenic mice, which express the Cre recombinase specifically in cardiomyocytes [25]. These knockout mice appeared healthy in the first several months although *PTPMT1* was nearly completely deleted from the heart (but not in Soleus and EDL) (Supplemental Figure 5A). No

obvious tissue morphological changes or fibrotic lesions were found in *PTPMT1* knockout hearts (Supplemental Figure 5B), confirming that PTPMT1-mediated metabolism is dispensable for the development of the heart. Echocardiography also showed normal heart function in 3-month-old *PTPMT1*$^{fl/fl}$*/MYH6-Cre*$^{+}$ mice, as evidenced by normal FS, EF, and E/A ratios (Supplemental Figure 5, C-E). Knockout mice did not exhibit any defects during treadmill exercises at 6 months of age (Supplemental Figure 5F). However, all *PTPMT1*$^{fl/fl}$*/MYH6-Cre*$^{+}$ knockout mice died at 10-16 months, and they often succumbed suddenly (Figure 5A) although their body weights were relatively normal. *PTPMT1* knockout hearts showed enlarged ventricular chambers. Severe structural damage in cardiac myocytes and tremendous fibrotic lesions were observed in the knockout hearts (Figure 5B). Immunostaining of cleaved caspase 3 illustrated increased apoptosis in *PTPMT1*$^{fl/fl}$*/MYH6-Cre*$^{+}$ cardiomyocytes as compared to control cells (Figure 5C). Echocardiography revealed a profound dilated cardiomyopathy and heart failure in *PTPMT1*$^{fl/fl}$*/MYH6-Cre*$^{+}$ mice, including both systolic and diastolic LV dilation, thinning of ventricular walls, depression of EF and FS, arrhythmias, and impaired myocardial contraction (Figure 5, D-J and Supplemental Video 2, A and B). Cardiac strain images demonstrated that the global function of *PTPMT1*$^{fl/fl}$*/MYH6-Cre*$^{+}$ hearts, as reflected by global longitudinal strain, was significantly decreased (Supplemental Figure 6, A and B), similar to that observed in *PTPMT1*$^{fl/fl}$*/CKMM-Cre*$^{+}$ mice.

Unlike those in younger knockout mice, total cellular ATP levels in 10 to 12-month-old *PTPMT1*$^{fl/fl}$*/MYH6-Cre*$^{+}$ hearts were decreased by half (Figure 6A), and the knockout cardiomyocytes exhibited pronounced energetic stress as demonstrated by a substantial increase in p-AMPK (T^{172}) and decrease in p-mTOR (S^{2448}) (Figure 6B). To determine the direct effects of PTPMT1 loss on

cardiomyocyte metabolism, we examined heart tissues isolated from young (3 months old) knockout mice before cardiomyocyte and mitochondria damages occurred. The mitochondrial content in these young *PTPMT1* knockout cardiac tissues was comparable to that in control tissues (Supplemental Figure 7A), and there were no changes in the expression levels of mitochondrial complexes (Supplemental Figure 7B). Moreover, no bioenergetic/metabolic stress was detected in the knockout cardiomyocytes at this age (Supplemental Figure 7C). However, like *PTPMT1* knockout skeletal muscle mitochondria (Figure 3, B-D), PTPMT1-ablated cardiac mitochondria also showed altered fuel selection – the utilization of pyruvate was decreased (Figure 6C), whereas the free fatty acid and glutamate utilization was increased in *PTPMT1*$^{fl/fl}$*/MYH6-Cre*$^{+}$ cardiac mitochondria (Figure 6, D and E). Intramitochondrial pyruvate levels in PTPMT1-ablated cardiac mitochondria decreased (Figure 6F) while acetyl-CoA levels were not changed (Supplemental Figure 7D), consistent with the metabolite data obtained from PTPMT1-depleted skeletal muscle mitochondria (Figure 3, F and H). Furthermore, acute production of α-KG from extramitochondrial pyruvate was decreased in the cardiac mitochondria lacking PTPMT1 (Figure 6G), although PDH activity in these mitochondria was not significantly affected (Figure 6H).

Oxidation of fatty acids in mitochondria yields much more ATP relative to carbohydrates (via pyruvate); however, fatty acid oxidation requires a greater rate of oxygen consumption for a given rate of ATP synthesis than carbohydrates. Such that the byproduct reactive oxygen species are increased when mitochondria switch to fatty acids for energy metabolism. Indeed, *PTPMT1* knockout heart tissues showed elevated overall cellular ROS levels even at 3 months (Figure 6I). Persistent oxidative stress can cause mitochondrial damage. Electron microscopic examination revealed that the myocardium of *PTPMT1*$^{fl/fl}$*/MYH6-Cre*$^{+}$ mice was distinguishable from that of *PTPMT1*$^{+/+}$*/MYH6-Cre*$^{+}$ control mice by

the structures of mitochondria at 6-8 months (Figure 6J). Similar to that observed in *PTPMT1* knockout skeletal muscle cells (Figure 2C), drastic accumulation of lipids or lipid intermediates was observed in 10-12-month-old *PTPMT1*$^{fl/fl}$*/MYH6-Cre*$^{+}$ cardiomyocytes (Figure 6K), which is likely responsible for the increased apoptosis and fibrillation in the knockout heart (Figure 5, B and C) due to the toxicity of excess lipids (lipotoxicity) [26,27].

PTPMT1 is dispensable for the liver and adipose tissues

Finally, to further determine whether PTPMT1-facilitated carbohydrate oxidation in mitochondria is also important for other important metabolic tissues, we generated liver-specific (*PTPMT1*$^{fl/fl}$*/ALB-Cre*$^{+}$) and fat-specific (*PTPMT1*$^{fl/fl}$*/Adipoq-Cre*$^{+}$) *PTPMT1* knockout mice by crossing *PTPMT1 floxed* mice [11] with *ALB-Cre* [28] and *Adipoq-Cre* [29] mice, which express Cre specifically in hepatocytes and adipocytes, respectively. In contrast to muscle/heart- and heart-specific knockout mice, liver-specific *PTPMT1* knockout mice were healthy without overt abnormalities. They had a normal lifespan. Their body weights, liver weights, and blood glucose levels under both feeding and fasting conditions were comparable to those in control animals (Supplemental Figure 8, A-D). Moreover, no significant differences were observed in glucose tolerance tests between *PTPMT1*$^{fl/fl}$*/ALB-Cre*$^{+}$ and control mice (Supplemental Figure 8E). Unlike muscle/heart- and heart-specific *PTPMT1* knockout mice in which prominent lipid accumulation was detected in muscle and cardiac myocytes, liver-specific *PTPMT1* knockout mice did not display this secondary effect in hepatocytes, and there was no evident tissue damage in the liver or a fatty liver phenotype (Supplemental Figure 8F). Similarly, adipocyte-specific *PTPMT1* knockout mice were also healthy. Their body weights and glucose tolerance were comparable to those of control animals (Supplemental Figure 9, A and B). No histological changes were observed in

PTPMT1 knockout white adipose and brown adipose tissues (Supplemental Figure 9C). The fact that *PTPMT1*$^{fl/fl}$/*ALB-Cre*$^{+}$ and *PTPMT1*$^{fl/fl}$/*Adipoq-Cre*$^{+}$ mice well tolerated PTPMT1 deficiency in hepatocytes or adipocytes suggests that the detrimental effects of PTPMT1 depletion-induced mitochondrial substrate shift are highly cell type-specific.

DISCUSSION

Mitochondrial flexibility in substrate selection is essential for maintaining cellular energy homeostasis in physiology and under stress; however, the regulatory mechanisms and its significance for various tissues and cell types remain poorly characterized [1]. In this study, we have identified an important role of the mitochondrial phosphatase PTPMT1 in maintaining mitochondrial flexibility. The loss of PTPMT1 decreased mitochondrial utilization of pyruvate, a key mitochondrial substrate derived from glucose, whereas fatty acid oxidation was enhanced (Figure 3C, Figure 6D). Importantly, this prolonged mitochondrial substrate shift causes oxidative stress and mitochondrial damage, ultimately leading to the accumulation of lipids/lipid intermediates in *PTPMT1* knockout skeletal muscle and cardiac myocytes. Excess lipids/lipid intermediates are known to be toxic to cardiomyocytes (lipotoxicity) [26,27]. The profound damages in *PTPMT1* knockout hearts and muscles that occurred subsequently were likely attributed to these accumulated lipids, although other factors, such as decreased anabolic activities (as demonstrated by diminished mTOR signaling) (Figure 2F, Figure 6B), could also contribute to these phenotypes. The mitochondrial and tissue damages that subsequently occurred, combined with the resulting energetic stress, finally led to muscle atrophy and heart failure in the knockout mice.

One of the important findings in this report is that persistent mitochondrial fuel switch from pyruvate to

fatty acids is detrimental for both cardiac and skeletal muscles despite the two tissues having different preferred energy sources. Glucose is the major energy source for skeletal muscles. It is used for energy production mainly in mitochondria in oxidative red muscles or through cytosolic glycolysis in glycolytic white muscles. Glucose is also the main energy source for the developing heart, but the adult heart primarily utilizes fatty acids to produce ATP, although the adult heart can also utilize glucose and lactate, the end product of glycolysis, as energy sources. Indeed, when mitochondrial utilization of pyruvate was inhibited by PTPMT1 depletion, heart dysfunction developed much later than skeletal muscle dysfunction. Interestingly, our data from these animal models suggest that efficient carbohydrate oxidation in mitochondria and balanced mitochondrial fuel selection are critically important for both oxidative and glycolytic muscles as well as the adult heart, but not for the development of the skeletal muscle and heart although PTPMT1 depletion took place during the embryonic stage. Undoubtedly, the late-onset phenotypes observed in the knockout mice over time was attributed to the metabolic defects arising from the loss of PTPMT1 in the embryos. Although PTPMT1 knockout muscle cells and cardiomyocytes initially maintained energy homeostasis through enhanced fatty acid and glutamate oxidation, along with metabolic adaptations or activation of alternative energy-producing pathways in the first few months, they eventually encountered substantial energy deficits. This was attributed to the subsequent occurrence of oxidative stress and mitochondrial damage.

PTPMT1 knockout hepatocytes or adipocytes did not display such secondary effects (mitochondria and cell damages). This is possibly because the requirement of carbohydrate oxidation for energy production in hepatocytes and adipocytes is lower than that in skeletal muscle cells and cardiomyocytes, and/or *PTPMT1* knockout hepatocytes and adipocytes did not need to uptake excessive fatty acids in the effort

to maintain energy homeostasis. Another possibility is that the capabilities of hepatocytes and adipocytes to process fatty acids and to clear lipid metabolites (through cholesterol synthesis and cholesterol exportation out of the cell) are much stronger than muscle cells and cardiomyocytes [30].

Another important finding in this report is that PTPMT1 plays a major role in governing the metabolic fate of pyruvate and maintaining mitochondrial flexible substrate utilization. Pyruvate is at the central branch point of mitochondrial oxidation and cytosolic glycolysis in glucose metabolism − It can enter the mitochondrion for oxidation or be reduced to lactate in the cytosol. Our data suggest that inhibited mitochondrial utilization of pyruvate is most likely responsible for the remodeled metabolism in *PTPMT1* knockout cells since ATP synthesis-driven oxygen consumption of PTPMT1-ablated mitochondria was greatly reduced with pyruvate as the sole substrate (Figure 3B, Figure 6C). Moreover, acute production of α-KG from extramitochondrial pyruvate was indeed decreased (Figure 3I, Figure 6G).

The precise mechanism by which PTPMT1 facilitates mitochondrial utilization/uptake of pyruvate remains to be further determined. PTPMT1 is localized to the inner mitochondrial membrane where pyruvate transporters reside. This phosphatase dephosphorylates phosphatidylinositol phosphates (PIPs) [11-13]. We have shown previously that PIPs directly promote fatty acid-induced activation of UCP2 [11]. UCP2, unlike UCP1, is a C4 metabolite transporter [14]. Elevated UCP2 activity inhibits mitochondrial oxidation of glucose but enhances cytosolic glycolysis although the underlying mechanisms remain unclear [15-18]. PTPMT1 depletion conceivably leads to the buildup of downstream PIP substrates in the mitochondrial inner membrane, which in turn remodel mitochondrial energy source selection by

enhancing UCP2 function [11] [UCP2 levels in PTPMT1-ablated mitochondria were not changed (Supplemental Figure 3A, 7B)]. It may also be possible that the accumulated PIPs directly inhibit the mitochondrial pyruvate transporter MPC. It is important to note that PTPMT1 was reported to be involved in the synthesis of cardiolipin [9] which is one of the major components of the mitochondrial inner membrane and that plays an important role in maintaining mitochondrial membrane stability and dynamics. Thus, it may also be possible that PTPMT1 depletion decreases mitochondrial pyruvate utilization through reduced cardiolipin synthesis. Comprehensive metabolomic analyses for *PTPMT1*-deleted cells would provide additional insights into the mechanisms underlying the metabolic alterations caused by PTPMT1 loss.

In summary, in this report we provide evidence that the mitochondria-based multi-functional phosphatase PTPMT1 plays an important role in facilitating mitochondrial utilization of pyruvate and maintaining mitochondrial flexibility for balanced substrate selection. Prolonged mitochondrial energy sources switch from carbohydrates to lipids such as that caused by PTPMT1 depletion is detrimental for the skeletal muscle and heart but not the liver and adipose, ultimately leading to muscle atrophy and heart failure.

MATERIALS AND METHODS

Mice

PTPMT1$^{fl/+}$ mice with the C57Bl/6 background were generated in our previous study [11]. *CKMM-Cre*$^{+}$ [19] (Stock# 006475), *MYH6-Cre*$^{+}$ [25] (Stock# 011038), *ALB-Cre*$^{+}$ [28] (Stock# 003574), and *Adipoq-Cre*$^{+}$ [29] (Stock# 010803) mice with the C57BL/6 background were purchased from the Jackson Laboratory. To avoid potential side effects of Cre, *PTPMT1*$^{+/+}$*/Cre*$^{+}$ mice were used as controls for *PTPMT1*$^{fl/fl}$*/Cre*$^{+}$

mice and the *Cre* transgene was hemizygous in both mouse types. In initial pilot experiments, we examined *PTPMT1*$^{+/+}$/*Cre*$^{+}$ mice and no defects were observed in these animals. Mice were kept under specific pathogen-free conditions in Case Western Reserve University Animal Resources Center and Emory University Division of Animal Resources. Mice of the same age, sex, and genotype were randomly grouped for subsequent analyses (investigators were not blinded). All animal procedures complied with the NIH Guidelines for the Care and Use of Laboratory Animals and were approved by the Institutional Animal Care and Use Committee.

Antibodies

The sources and catalog numbers of the antibodies utilized in this study are listed below.

Antibodies	SOURCE	Cat. #
Phospho-AMPKα (Thr^{172}) (40H9) Rabbit mAb	Cell Signaling Technology	2535
AMPKα (D5A2) Rabbit mAb	Cell Signaling Technology	5831
Phospho-Acetyl-CoA Carboxylase (Ser^{79}) (D7D11) Rabbit mAb (p-ACC)	Cell Signaling Technology	11818
Acetyl-CoA Carboxylase (C83B10) Rabbit mAb (ACC)	Cell Signaling Technology	3676
Phospho-mTOR (Ser^{2448}) (D9C2) XP®Rabbit mAb	Cell Signaling Technology	5536
mTOR (7C10) Rabbit mAb	Cell Signaling Technology	2983
Phospho-p70 S6 Kinase (Thr^{389}) (108D2) Rabbit mAb	Cell Signaling Technology	9234
p70 S6 Kinase (49D7) Rabbit mAb	Cell Signaling Technology	2708
Phospho-S6 Ribosomal Protein (Ser$^{240/244}$) (D68F8) XP® Rabbit mAb	Cell Signaling Technology	5364
S6 Ribosomal Protein (5G10) Rabbit mAb	Cell Signaling Technology	2217
β-actin mouse Ab	Santa Cruz Biotechnology	SC-47778

Phospho-4E-BP1 (Thr$^{37/46}$) (236B4) Rabbit mAb	Cell Signaling Technology	2855
Phospho-Akt (Thr^{308}) (D25E6) XP® Rabbit mAb	Cell Signaling Technology	13038
Phospho-Akt (Ser^{473}) (D9E) XP®Rabbit mAb	Cell Signaling Technology	4060
Akt (pan) (C67E7) Rabbit mAb	Cell Signaling Technology	4691
p-Erk Rabbit Ab	Santa Cruz Biotechnology	SC7383
Erk Rabbit Ab	Cell Signaling Technology	9102
MPC1 (D2L9I) Rabbit mAb	Cell Signaling Technology	14462
MPC2 (D4I7G) Rabbit mAb	Cell Signaling Technology	46141
Total OXPHOS Rodent WB Antibody Cocktail Mouse Ab	Abcam	ab110413
UCP2 Rabbit Ab	Santa Cruz Biotechnology	SC6525
LC3 Rabbit Ab	Novus Biologicals	NB100-2331

Wire hang test

Maximal muscular strength of mouse forelimbs was assessed by wire hang tests following a standard protocol. Mice were allowed to grasp and hang on a wire with forelimbs. Time duration when the mouse was able to suspend before falling was recorded. Three trials were carried out for each mouse. The average time was normalized against body weight. Values of control mice were set to 100%.

Treadmill exercise test

Treadmill exercise tests were conducted following the protocol previously reported by trained personnel at Case Western Reserve University Mouse Metabolic Phenotyping Center Analytical Core [31,32]. Adjustable parameters on the treadmill include belt speed (0-99 m/min) and angle of inclination (0-45”). After acclimation for 1 hour, 2.5 m/min incremental increases in treadmill belt speed and 2’ increments in

an angle of inclination were performed every 3 min until the mouse exhibited signs of exhaustion. Exhaustion was defined as the mouse spending >50% of the time or X5 sec consecutively on the shock grid. The maximum speed and duration of the run were recorded at the time of exhaustion.

Ex vivo muscle contractility assay

Intact Soleus and EDL isolated from mice were used for the collection of isometric force data using an eight-chamber system [12,33]. Data were analyzed with ADInstruments PowerLab software customized for these experiments. Muscles were first equilibrated for 20 min to mimic conditions of normal activity (low duty cycle, ∼1%). Muscles were then subjected to the length-force relationship test to determine the optimal length at which maximal force is achieved. Muscles were stimulated with frequencies ranging from 1 to 130 Hz to generate force *versus* frequency relationships. From these relationships, the frequency producing maximal tetanic force (T_{max}) was then used for the rest of the experiments. Muscles were stimulated every minute with T_{max} for 5–10 min to assure that the preparation was stable at which point the tissue bathing buffer was replaced with one containing 0 mM Ca^{2+} + 0.1 mM EGTA. The muscles were then stimulated every minute at T_{max} to determine the impact of the removal of external calcium on muscle force. After 20 min, the 0 mM Ca^{2+} buffer was washed out and replaced by a buffer containing 2.5 mM Ca^{2+}, and the muscles were stimulated every minute for 20 min at T_{max} to allow for force recovery. After force measurement protocols, muscle dimensions and masses were measured for the determination of cross-sectional normalized forces (relative force). Muscle force was reported as absolute force (mN) and force normalized to the following muscle physiological cross-sectional area (PCSA, N/cm2) equation as previously reported [34,35] with a small modification in that in our final length calculation, we considered the length to weight ratio of muscle fibers for stretched muscles (tendon-to-

tendon) of *ex vivo* muscles in contractility chambers [36] as the actual muscle fiber size was smaller than the length of the measured stretched muscle. Since the PCSA is very sensitive to length, by adjusting to the length of the muscle fiber, force estimation was more precise. Thus, our final formula was: Muscle force (N/cm2) = (force (g) x (muscle length (cm) x 0.75 (EDL) or 0.85 (Soleus) x 1.06 (muscle density))/(muscle weight (g) x 0.00981).

Echocardiography

Echocardiographic studies were performed by trained investigators at Emory University Department of Pediatrics Animal Physiology Core as previously reported [37,38]. Mice were anesthetized with 1-2% isoflurane/100% oxygen continuously and positioned on a warming platform set to 37°C. The heart rate was controlled at 360-460 beats per minute to standardize recordings. ECG and respiratory rate were monitored for physiological assessment while scanning. A Vevo 2100 digital high-frequency ultrasound system (FujiFilm Visualsonics Inc, Toronto, ON, Canada) equipped with an MS400, 30-MHz transducer was used to acquire the images. Interventricular septal thicknesses (IVS), left ventricular internal dimensions (LVID) and posterior wall thicknesses (LVPW) at diastole and systole (IVS-d, LVID-d, LVPW-d and IVS-s, LVID-s, LVPW-s) were measured from M-mode images in both parasternal long axis and short-axis views. Left ventricle volume at diastole and systole (LV Vol-d, LV Vol-s), left ventricular ejection fraction (LVEF) and left ventricular fractional shortening (LVFS) were calculated as the following formula (Vevo 2100 Workstation Software VisualSonics INC, Toronto, ON, Canada): LV Vol-d(ul) = [(7.0 /(2.4 + LVID-d)] * LVID-d^3); LV Vol-d(ul) = [(7.0 /(2.4 + LVID-s)] * LVID-s^3); EF (%) = 100 * [(LV Vol-d – LV Vol-s) / LV Vol-d]; FS (%) = 100 * [(LVID-d – LVID-s) / LVID-d]. The mitral valve flow Doppler velocities were measured by the apical four-chamber view. Early (E) and late (A)

mitral valve inflow velocity and mitral valve E to A ratios (MV E/A) were also obtained.

Echocardiographic speckle-tracking based strain measurement was also performed using the VevoStrain^{TM} application (VisualSonics Vevo 2100 Imaging System, FujiFilm VisualSonics, Inc, Toronto, ON, Canada) which produces velocity strain and time-to-peak analyses on myocardial wall images. The B-Mode cine loop was acquired for Vevo Strain analysis. The qualified consecutive cardiac cycles were selected between one respiration cycle and the next in the EKG panel. Both endocardium and epicardium were traced simultaneously and semi-automatically at the parasternal long-axis view. VevoStrain builds the dynamic LV wall trace for all frames in the cine loop. Velocity, displacement, strain, and strain rate data were calculated based on a speckling-tracking algorithm provided by the Vevo software. Data on overall cardiac tissue performance, segmental time-to-peak, and segmental phase quantification were also collected.

Intracellular ATP quantification

Skeletal muscle and heart tissues were lysed in lysis buffer [Tris-HCl (50 mM), pH 7.4, NP-40 (1%), Na-deoxycholate (0.25%), NaCl (150 mM), EDTA (1 mM), NaF (1 mM), Na_3VO_4 (1 mM), PMSF (1 mM), and Aprotinin/Leupeptin (10 µg/ml)] for 30 min. Samples were then centrifuged (10,000g) for 10 min, and the supernatants were collected. Total ATP levels were assessed using an ATP bioluminescence assay kit (Sigma, St. Louis, MO), following the instructions provided by the manufacturer. ATP levels were normalized against tissue weights or protein contents in the samples.

Measurement of respiration in isolated mitochondria

Mitochondria were freshly isolated from skeletal muscle and heart tissues. Respiration of mitochondria was measured using a Seahorse XF24 analyzer as described previously [39]. Mitochondria (10 µg of protein) were plated in each well of a XF24 plate in 50 µl 1x Mitochondrial Assay Solution (MAS), pH 7.4 [Sucrose (70 mM), Mannitol (220 mM), KH_2PO_4 (5 mM), $MgCl_2$ (5 mM), HEPES (2 mM), EGTA (1 mM), and fatty acids-free BSA (0.2%)]. XF24 plates were centrifuged at 4°C for 20 min at 2,000g, and then 450 µl of MAS containing 5 mM pyruvate/5 mM malate, 5 mM glutamate/5 mM malate, 40 µM palmitoyl-CoA/40 µM carnitine/5 mM malate, or 10 mM succinate was added to each well. Plates were incubated at 37°C in an incubator for 8–10 min. Oxygen consumption rates (OCRs) were measured under basal conditions in the presence of ADP (4 mM), the ATP synthase inhibitor oligomycin (1.5 µM), the mitochondrial uncoupling compound carbonylcyanide-4-trifluorometh-oxyphenylhydrazone (FCCP, 4 µM), and the electron transport chain inhibitor rotenone (1 µM).

Measurement of respiration in fresh muscle tissues

OCRs of muscle tissues were measured using a Seahorse XF24 analyzer and Seahorse XF24 Islet Capture Microplates (Agilent, 101122-100) as described previously [40]. Briefly, tibialis anterior muscles were dissected into 3 x 1 mm cross-sections with a biopsy punch (3 mm diameter). The tissue sections were incubated for 1 hour in DMEM supplemented with 10 mM glucose, 2 mM L-glutamine, and 1 mM sodium pyruvate. Tissue OCRs were measured at the basal level and following the addition of oligomycin (8 µM), FCCP (4 µM), and antimycin A/rotenone (1 µM). Following OCR measurements, tissues were dried at 60 °C for 48 hours. All tissue OCR measurements were then normalized against dry tissue weights.

Mitochondrial pyruvate dehydrogenase (PDH) activity assay, pyruvate, acetyl-CoA, and α-ketoglutarate (α-KG) measurements

Mitochondria were freshly isolated from skeletal muscle/heart tissues and washed twice with MAS. Mitochondrial pellets were lysed in [Tris-HCl (pH 7.4, 50 mM), NP-40 (1%), Na-deoxycholate (0.25%), NaCl (150 mM), EDTA (1 mM), NaF (1 mM), Na_3VO_4 (1 mM), PMSF (1 mM), aprotinin/leupeptin (10 μg/ml)]. Lysates were subjected to the PDH activity assay and pyruvate, acetyl-CoA, and α-KG measurements using PDH activity colorimetric assay, pyruvate assay, acetyl-CoA assay, and α-KG assay kits purchased from BioVision following the manufacturer's instructions.

Histological and transmission electron microscopic (TEM) examination

Freshly dissected skeletal muscle and heart tissues were embedded in Optimal Cutting Temperature (OCT) compound (Tissue-Tek) and frozen at -80°C. Slides were stained for Hematoxylin and Eosin (H&E), Masson's trichrome, and Oil Red O. For TEM analyses, mice were perfused with 3% paraformaldehyde, 1.5% glutaraldehyde, 100 mM cacodylate (pH 7.4), and 2.5% sucrose. Skeletal muscle and heart tissues were postfixed for 1 hour and then processed for TEM examination.

Tissue reactive oxygen species (ROS) determination

Freshly dissected heart tissues were embedded in Optimal Cutting Temperature (OCT) compound (Tissue-Tek) and immediately placed on crushed dry ice. Frozen sections were prepared at 8 μm thickness. After being rinsed in pure H_2O for 30 seconds to wash out OCT compound, slides were stained with 5 μM dihydroethidium (DHE) at room temperature in dark for 15 min. Slides were washed with deionized H_2O for 1 min three times and visualized immediately using a fluorescence microscope. DHE-

derived 2-OH-E^+, a specific adduct of cellular superoxide, was visualized with a red excitation filter. Equal exposure times were applied to all slides. Fluorescence intensities were measured by ImageJ software.

Immunoblotting

Skeletal muscle and heart tissues were lysed in RIPA buffer (50 mM Tris-HCl pH 7.4, 1% NP-40, 0.25% Na-deoxycholate, 150 mM NaCl, 1 mM EDTA, 1 mM NaF, 1 mM Na_3VO_4, 10 μg/mL leupeptin, 10 μg/mL aprotinin, and 1 mM PMSF). Lysates (50 μg) were resolved by SDS-PAGE followed by immunoblotting with the indicated antibodies following standard procedures.

Statistics

Data are presented as mean ± S.D. of all mice analyzed (i.e., biological replicates) in multiple experiments. Tissues, mitochondria, etc. that were analyzed were isolated from single individual mice (not pooled). Statistical significance was determined using unpaired two-tailed Student's *t* test. * $p < 0.05$; ** $p < 0.01$; *** $p < 0.001$. N.S. indicates not significant.

Acknowledgements

We are grateful for the technical assistance provided by Julian Vallejo and the services provided by Children's Healthcare of Atlanta and Emory University's Animal Physiology Core, and Case Mouse Metabolic Phenotyping Center. This work was supported by the National Institutes of Health grants HL130995 and HL162725 (to C.K.Q.).

Author contributions

H.Z., Q.L., S.L., Z.L., M.B., D.W., D.P., A.R., and M.P. conducted the research and summarized the data. M.B., C.X., M.P., X.Z., M.N.W., and M.K.J. provided critical advice, discussed the work, and edited the manuscript. M.B. designed contractility experiments. C.K.Q. designed other experiments and directed the entire study. H.Z., Q.L., S.L., and C.K.Q. wrote the manuscript with the input from the other authors.

Competing financial interests

The authors declare no competing financial interests.

REFERENCES

1 Smith, R. L., Soeters, M. R., Wust, R. C. I. & Houtkooper, R. H. Metabolic Flexibility as an Adaptation to Energy Resources and Requirements in Health and Disease. *Endocr Rev* **39**, 489-517, doi:10.1210/er.2017-00211 (2018).

2 Bertero, E. & Maack, C. Metabolic remodelling in heart failure. *Nat Rev Cardiol* **15**, 457-470, doi:10.1038/s41569-018-0044-6 (2018).

3 Brown, D. A. *et al.* Expert consensus document: Mitochondrial function as a therapeutic target in heart failure. *Nat Rev Cardiol* **14**, 238-250, doi:10.1038/nrcardio.2016.203 (2017).

4 Nabben, M., Luiken, J. & Glatz, J. F. C. Metabolic remodelling in heart failure revisited. *Nat Rev Cardiol* **15**, 780, doi:10.1038/s41569-018-0115-8 (2018).

5 Schulze, P. C., Drosatos, K. & Goldberg, I. J. Lipid Use and Misuse by the Heart. *Circ Res* **118**, 1736-1751, doi:10.1161/CIRCRESAHA.116.306842 (2016).

6 Pagliarini, D. J. *et al.* Involvement of a mitochondrial phosphatase in the regulation of ATP production and insulin secretion in pancreatic beta cells. *Mol Cell* **19**, 197-207, doi:10.1016/j.molcel.2005.06.008 (2005).

7 Balla, T. Phosphoinositide-derived messengers in endocrine signaling. *J Endocrinol* **188**, 135-153 (2006).

8 Gamper, N. & Shapiro, M. S. Regulation of ion transport proteins by membrane phosphoinositides. *Nat Rev Neurosci* **8**, 921-934 (2007).

9 Zhang, J. *et al.* Mitochondrial phosphatase PTPMT1 is essential for cardiolipin biosynthesis. *Cell Metab* **13**, 690-700, doi:10.1016/j.cmet.2011.04.007 (2011).

10 Shen, J. *et al.* A critical role of mitochondrial phosphatase Ptpmt1 in embryogenesis reveals a mitochondrial metabolic stress-induced differentiation checkpoint in embryonic stem cells. *Mol Cell Biol* **31**, 4902-4916, doi:10.1128/MCB.05629-11 (2011).

11 Yu, W. M. *et al.* Metabolic regulation by the mitochondrial phosphatase PTPMT1 is required for hematopoietic stem cell differentiation. *Cell Stem Cell* **12**, 62-74, doi:10.1016/j.stem.2012.11.022 (2013).

12 Shen, J. *et al.* Deficiency of MIP/MTMR14 phosphatase induces a muscle disorder by disrupting Ca(2+) homeostasis. *Nat Cell Biol* **11**, 769-776, doi:10.1038/ncb1884 (2009).

13 Pagliarini, D. J., Worby, C. A. & Dixon, J. E. A PTEN-like phosphatase with a novel substrate specificity. *J Biol Chem* **279**, 38590-38596 (2004).

14 Vozza, A. *et al.* UCP2 transports C4 metabolites out of mitochondria, regulating glucose and glutamine oxidation. *Proc Natl Acad Sci U S A* **111**, 960-965, doi:10.1073/pnas.1317400111 (2014).

15 Bouillaud, F. UCP2, not a physiologically relevant uncoupler but a glucose sparing switch impacting ROS production and glucose sensing. *Biochim Biophys Acta* **1787**, 377-383, doi:S0005-2728(09)00010-3 [pii]
10.1016/j.bbabio.2009.01.003 (2009).

16 Diano, S. & Horvath, T. L. Mitochondrial uncoupling protein 2 (UCP2) in glucose and lipid metabolism. *Trends Mol Med* **18**, 52-58, doi:S1471-4914(11)00161-4 [pii]
10.1016/j.molmed.2011.08.003 (2012).

17 Pecqueur, C. *et al.* Uncoupling protein-2 controls proliferation by promoting fatty acid oxidation and limiting glycolysis-derived pyruvate utilization. *FASEB J* **22**, 9-18, doi:fj.07-8945com [pii]
10.1096/fj.07-8945com (2008).

18 Samudio, I., Fiegl, M. & Andreeff, M. Mitochondrial uncoupling and the Warburg effect: molecular basis for the reprogramming of cancer cell metabolism. *Cancer research* **69**, 2163-2166, doi:0008-5472.CAN-08-3722 [pii]

10.1158/0008-5472.CAN-08-3722 (2009).

19 Bruning, J. C. *et al.* A muscle-specific insulin receptor knockout exhibits features of the metabolic syndrome of NIDDM without altering glucose tolerance. *Mol Cell* **2**, 559-569 (1998).

20 Hardie, D. G. AMPK: positive and negative regulation, and its role in whole-body energy homeostasis. *Current opinion in cell biology* **33**, 1-7, doi:10.1016/j.ceb.2014.09.004 (2015).

21 Liang, J. & Mills, G. B. AMPK: a contextual oncogene or tumor suppressor? *Cancer research* **73**, 2929-2935, doi:10.1158/0008-5472.CAN-12-3876 (2013).

22 Bentzinger, C. F. *et al.* Skeletal muscle-specific ablation of raptor, but not of rictor, causes metabolic changes and results in muscle dystrophy. *Cell Metab* **8**, 411-424, doi:10.1016/j.cmet.2008.10.002 (2008).

23 Risson, V. *et al.* Muscle inactivation of mTOR causes metabolic and dystrophin defects leading to severe myopathy. *J Cell Biol* **187**, 859-874, doi:10.1083/jcb.200903131 (2009).

24 Zheng, H. *et al.* Mitochondrial oxidation of the carbohydrate fuel is required for neural precursor/stem cell function and postnatal cerebellar development. *Sci Adv* **4**, eaat2681, doi:10.1126/sciadv.aat2681 (2018).

25 Agah, R. *et al.* Gene recombination in postmitotic cells. Targeted expression of Cre recombinase provokes cardiac-restricted, site-specific rearrangement in adult ventricular muscle in vivo. *J Clin Invest* **100**, 169-179, doi:10.1172/JCI119509 (1997).

26 Goldberg, I. J., Trent, C. M. & Schulze, P. C. Lipid metabolism and toxicity in the heart. *Cell Metab* **15**, 805-812, doi:10.1016/j.cmet.2012.04.006 (2012).

27 Huss, J. M. & Kelly, D. P. Mitochondrial energy metabolism in heart failure: a question of balance. *J Clin Invest* **115**, 547-555, doi:10.1172/JCI24405 (2005).

28 Postic, C. *et al.* Dual roles for glucokinase in glucose homeostasis as determined by liver and pancreatic beta cell-specific gene knock-outs using Cre recombinase. *J Biol Chem* **274**, 305-315 (1999).

29 Eguchi, J. *et al.* Transcriptional control of adipose lipid handling by IRF4. *Cell Metab* **13**, 249-259, doi:10.1016/j.cmet.2011.02.005 (2011).

30 Sinha, R. A., Singh, B. K. & Yen, P. M. Direct effects of thyroid hormones on hepatic lipid metabolism. *Nat Rev Endocrinol* **14**, 259-269, doi:10.1038/nrendo.2018.10 (2018).

31 Desai, K. H. *et al.* Cardiovascular indexes in the mouse at rest and with exercise: new tools to

study models of cardiac disease. *Am J Physiol* **272**, H1053-1061, doi:10.1152/ajpheart.1997.272.2.H1053 (1997).

32 Shechtman, O. & Talan, M. I. Effect of exercise on cold tolerance and metabolic heat production in adult and aged C57BL/6J mice. *J Appl Physiol (1985)* **77**, 2214-2218, doi:10.1152/jappl.1994.77.5.2214 (1994).

33 Thornton, A. M. *et al.* Store-operated Ca(2+) entry (SOCE) contributes to normal skeletal muscle contractility in young but not in aged skeletal muscle. *Aging (Albany NY)* **3**, 621-634, doi:10.18632/aging.100335 (2011).

34 de Paula Brotto, M. *et al.* Hypoxia/fatigue-induced degradation of troponin I and troponin C: new insights into physiologic muscle fatigue. *Pflugers Arch* **442**, 738-744 (2001).

35 Park, K. H. *et al.* Ex vivo assessment of contractility, fatigability and alternans in isolated skeletal muscles. *J Vis Exp*, e4198, doi:10.3791/4198 (2012).

36 Kitase, Y. *et al.* beta-aminoisobutyric Acid, l-BAIBA, Is a Muscle-Derived Osteocyte Survival Factor. *Cell Rep* **22**, 1531-1544, doi:10.1016/j.celrep.2018.01.041 (2018).

37 Winterberg, P. D., Jiang, R., Maxwell, J. T., Wang, B. & Wagner, M. B. Myocardial dysfunction occurs prior to changes in ventricular geometry in mice with chronic kidney disease (CKD). *Physiol Rep* **4**, doi:10.14814/phy2.12732 (2016).

38 Agarwal, U. *et al.* Age-Dependent Effect of Pediatric Cardiac Progenitor Cells After Juvenile Heart Failure. *Stem Cells Transl Med* **5**, 883-892, doi:10.5966/sctm.2015-0241 (2016).

39 Rogers, G. W. *et al.* High throughput microplate respiratory measurements using minimal quantities of isolated mitochondria. *PLoS One* **6**, e21746, doi:10.1371/journal.pone.0021746 (2011).

40 Shintaku, J. *et al.* MyoD Regulates Skeletal Muscle Oxidative Metabolism Cooperatively with Alternative NF-kappaB. *Cell Rep* **17**, 514-526, doi:10.1016/j.celrep.2016.09.010 (2016).

Figure Legends

Figure 1. Deletion of *PTPMT1* from skeletal muscles results in defective contractility and progressive muscle atrophy. (**A**) Representative 8-month-old of *PTPMT1*$^{fl/fl}$*/CKMM-Cre*$^{+}$ and *PTPMT1*$^{+/+}$*/CKMM-Cre*$^{+}$ mice, and hind limbs and hearts dissected from these mice were photographed. EDL and Soleus (n=8 mice/genotype), and heart (n=4 mice/genotype) weights were measured. *PTPMT1* mRNA levels in EDL, Soleus, and heart tissues were determined by quantitative reverse transcription PCR (qRT-PCR) (n=4 mice/genotype). (**B**) Skeletal muscle sections prepared from 8-month-old *PTPMT1*$^{+/+}$*/CKMM-Cre*$^{+}$ and *PTPMT1*$^{fl/fl}$*/CKMM-Cre*$^{+}$ mice were processed for H&E staining and Masson's Trichrome staining. One representative image from 3 mice/genotype is shown. (**C**) Six-month-old *PTPMT1*$^{+/+}$*/CKMM-Cre*$^{+}$ and *PTPMT1*$^{fl/fl}$*/CKMM-Cre*$^{+}$ mice (n=7/genotype) were subjected to wire hang tests. Relative forelimb muscle strength was determined. (**D** and **E**) Seven to eight-month-old *PTPMT1*$^{+/+}$*/CKMM-Cre*$^{+}$ (n=5 males and 5 females) and *PTPMT1*$^{fl/fl}$*/CKMM-Cre*$^{+}$ (n=3 males and 5 females) mice were assessed by treadmill exercise tests as described in Materials and Methods. Maximum speed (**D**) and duration of the run (**E**) were recorded. (**F** and **G**) Soleus (**F**) and EDL (**G**) dissected from 7 to 8-month-old *PTPMT1*$^{+/+}$*/CKMM-Cre*$^{+}$ and *PTPMT1*$^{fl/fl}$*/CKMM-Cre*$^{+}$ mice (n=3 mice, 6 muscles/genotype) were subjected to *ex vivo* isometric force measurements. Specific contractile forces produced at the indicated frequencies of stimulation were normalized to the physiological cross-sectional area. Shown on the left are representative absolute forces produced at 1, 10, and 100 Hz. * $p < 0.05$.

Figure 2. PTPMT1 loss ultimately leads to abnormal mitochondrial distribution, structural damage, and bioenergetic stress in skeletal muscles. (**A**) Skeletal muscle sections prepared from 6-month-old *PTPMT1*$^{+/+}$*/CKMM-Cre*$^{+}$ and *PTPMT1*$^{fl/fl}$*/CKMM-Cre*$^{+}$ mice were processed for Gömöri trichrome staining. One representative image from 3 mice/genotype is shown. (**B**) Soleus and EDL dissected from 8-month-old *PTPMT1*$^{fl/fl}$*/CKMM-Cre*$^{+}$ and *PTPMT1*$^{+/+}$*/CKMM-Cre*$^{+}$ mice were processed for transmission electron microscopic examination. One representative image from 3 mice/genotype is shown. (**C**) Skeletal muscle sections prepared from 6-month-old *PTPMT1*$^{+/+}$*/CKMM-Cre*$^{+}$ and *PTPMT1*$^{fl/fl}$*/CKMM-Cre*$^{+}$ mice were processed for Oil Red O staining to visualize lipids. One representative picture from 3 mice/genotype is shown. (**D**) Total DNA was extracted from Soleus and EDL dissected from 8-month-old *PTPMT1*$^{fl/fl}$*/CKMM-Cre*$^{+}$ and *PTPMT1*$^{+/+}$*/CKMM-Cre*$^{+}$ mice (n=3/genotype). Mitochondrial content was estimated by comparing the mitochondrial gene cytochrome B DNA levels to the nuclear gene 18S DNA levels by qPCR. (**E**) Total ATP levels in Soleus and EDL dissected from 8-month-old *PTPMT1*$^{fl/fl}$*/CKMM-Cre*$^{+}$ and *PTPMT1*$^{+/+}$*/CKMM-Cre*$^{+}$ mice (n=6/genotype) were determined. (**F**) Whole cell lysates prepared from the Soleus and EDL isolated from 7-month-old *PTPMT1*$^{fl/fl}$*/CKMM-Cre*$^{+}$ and their control mice were examined by immunoblotting with the indicated antibodies. Representative results from 3 mice/genotype are shown.

Figure 3. PTPMT1 ablation impairs mitochondrial utilization of pyruvate, whereas the fatty acid utilization is enhanced. (**A**) Muscle cross-sections prepared with biopsy punches from *PTPMT1*$^{fl/fl}$*/CKMM-Cre*$^{+}$ and *PTPMT1*$^{+/+}$*/CKMM-Cre*$^{+}$ mice (n=4/genotype) at 4 months of age were measured for OCRs at the basal level and following the addition of oligomycin (8 μM),

FCCP (4 μM), and antimycin A/rotenone (1 μM). (**B**-**E**) Mitochondria were isolated from the skeletal muscles dissected from *PTPMT1*$^{fl/fl}$*/CKMM-Cre*$^{+}$ and *PTPMT1*$^{+/+}$*/CKMM-Cre*$^{+}$ mice (n=3/genotype) at 3 months of age. Mitochondrial oxygen consumption (10 μg of mitochondrial protein) was measured in the presence of pyruvate (5 mM)/malate (5 mM) (**B**), palmitoyl-CoA (40 μM)/carnitine (40 μM)/malate (5 mM) (**C**), glutamate (5 mM)/malate (5 mM) (**D**), or succinate (10 mM) (**E**), following the addition of ADP (4 mM), oligomycin (1.5 μM), FCCP (4 μM), and antimycin A/rotenone (1 μM). Experiments were repeated three times with three independent pairs of mice. Similar results were obtained in each experiment. (**F**-**H**) Levels of pyruvate (**F**), α-KG (**G**), and acetyl-CoA (**H**) in the lysates of the mitochondria isolated from the above skeletal muscles were measured (n=6/genotype). (**I**) Mitochondria freshly isolated from the skeletal muscles of *PTPMT1*$^{fl/fl}$*/CKMM-Cre*$^{+}$ and *PTPMT1*$^{+/+}$*/CKMM-Cre*$^{+}$ mice (n=4/genotype) were washed three times in MAS buffer. The mitochondria were then incubated with pyruvate (5 mM)/malate (5 mM) and ADP (4 mM) at 37°C. Five min later, mitochondria were collected, washed, and lysed. α-KG levels in the mitochondrial lysates were measured. (**J**) Pyruvate dehydrogenase (PDH) activities in the mitochondrial lysates were determined (n=5-6 mice/genotype). (**K**) *MYH4, MYH2, and MYH7* mRNA levels in the skeletal muscles dissected from 3-month-old *PTPMT1*$^{+/+}$*/CKMM-Cre*$^{+}$ and *PTPMT1*$^{fl/fl}$*/CKMM-Cre*$^{+}$ mice (n=4/genotype) were determined by qRT-PCR.

Figure 4. *PTPMT1*$^{fl/fl}$*/CKMM-Cre*$^{+}$ mice manifest late-onset cardiac dysfunction. (**A**) Heart tissue sections prepared from 12-month-old *PTPMT1*$^{+/+}$*/CKMM-Cre*$^{+}$ and *PTPMT1*$^{fl/fl}$*/CKMM-Cre*$^{+}$ mice were processed for H&E staining. One representative image from 3 mice/genotype is

shown. (**B**-**F**) Cardiac morphology and function of 12-month-old *PTPMT1*$^{+/+}$*/CKMM-Cre*$^{+}$ and *PTPMT1*$^{fl/fl}$*/CKMM-Cre*$^{+}$ mice (n=5/genotype) were examined by echocardiography. Representative long-axis views in M-mode echocardiographic tracing of LV are shown (**B**). LV FS (**C**) and LV ejection fraction (EF) (**D**) were determined. Representative pulsed-wave Doppler recordings of mitral valve inflow are shown (**E**). Ratios of peak velocity of early to late filling of mitral inflow (E/A) were determined (**F**).

Figure 5. Deletion of *PTPMT1* from the heart ultimately leads to dilated cardiomyopathy and heart failure. (**A**) Kaplan-Meier survival curves of *PTPMT1*$^{fl/fl}$*/MYH6-Cre*$^{+}$ (n=18) and *PTPMT1*$^{+/+}$*/MYH6-Cre*$^{+}$ mice (n=20). (**B**) Heart tissue sections prepared from 10 to 12-month-old *PTPMT1*$^{fl/fl}$*/MYH6-Cre*$^{+}$ and *PTPMT1*$^{+/+}$*/MYH6-Cre*$^{+}$ mice (n=4/genotype) were processed for H&E staining and Masson's Trichrome staining. Representative images are shown. (**C**) Heart tissue sections prepared from 11-month-old *PTPMT1*$^{fl/fl}$*/MYH6-Cre*$^{+}$ and *PTPMT1*$^{+/+}$*/MYH6-Cre*$^{+}$ mice were processed for immunofluorescence staining for cleaved caspase 3 followed by DAPI counterstaining. One representative image from 3 mice/genotype is shown. (**D**-**J**) Eleven to twelve-month-old *PTPMT1*$^{fl/fl}$*/MYH6-Cre*$^{+}$ and *PTPMT1*$^{+/+}$*/MYH6-Cre*$^{+}$ mice (n=5/genotype) were examined by echocardiographic evaluation of ventricular function. Representative long- (upper panel) and short- (lower panel) axis views in M-mode echocardiographic tracing of LV (**D**), and pulsed-wave Doppler recordings of mitral valve inflow (**E**) are shown. Left ventricular internal diameters at diastole (LVID-d) and systole (LVID-s) were measured (**F**). LV ejection fraction (EF) and fractional shortening (FS) (**G**), ratios of peak velocity of early to late filling of mitral inflow (E/A) (**H**), the thickness of LV anterior wall at the

end of diastole (LVAW-d) and the end of systole (LVAW-s) (**I**), and thickness of LV posterior wall at the end of diastole (LVPW-d) and at the end of systole (LVPW-s) (**J**) were determined.

Figure 6. PTPMT1 deficiency causes mitochondrial substrate shift and oxidative stress, leading to mitochondrial damage and lipid accumulation in *PTPMT1* knockout cardiomyocytes. (**A**) Total ATP levels in the heart tissues dissected from *PTPMT1*$^{fl/fl}$*/MYH6-Cre*$^{+}$ and *PTPMT1*$^{+/+}$*/MYH6-Cre*$^{+}$ mice at the indicated ages (n=5 mice/genotype). (**B**) Whole cell lysates prepared from the heart tissues of 10 to 12-month-old *PTPMT1*$^{fl/fl}$*/MYH6-Cre*$^{+}$ and *PTPMT1*$^{+/+}$*/MYH6-Cre*$^{+}$ mice were examined by immunoblotting with the indicated antibodies. Representative results from 3 mice/genotype are shown. (**C**-**E**) Oxygen consumption of the mitochondria isolated from the heart tissues of 2 to 3-month-old *PTPMT1*$^{fl/fl}$*/MYH6-Cre*$^{+}$ and *PTPMT1*$^{+/+}$*/MYH6-Cre*$^{+}$ mice (n=3/genotype) was measured in the presence of pyruvate (5 mM)/malate (5 mM) (**C**), palmitoyl-CoA (40 μM)/carnitine (40 μM)/malate (5 mM) (**D**), or glutamate (5 mM)/malate (5 mM) (**E**), following the addition of ADP (4 mM), oligomycin (1.5 μM), FCCP (4 μM), and antimycin A/rotenone (1 μM). OCRs at basal levels, in response to ADP addition, and maximal reserve capabilities were determined. (**F**) Levels of pyruvate in the lysates of the cardiac mitochondria isolated from 2 to 3-month-old *PTPMT1*$^{fl/fl}$*/MYH6-Cre*$^{+}$ and *PTPMT1*$^{+/+}$*/MYH6-Cre*$^{+}$ mice (n=6/genotype) were determined. (**G** and **H**) Mitochondria isolated above were washed three times in MAS buffer and then incubated with pyruvate (5 mM)/malate (5 mM) and ADP (4 mM) at 37°C. Five min later, the mitochondria were collected, washed, and lysed. α-KG levels in the mitochondrial lysates were measured (n=4 mice/genotype) (**G**). Pyruvate dehydrogenase (PDH) activities in the mitochondrial lysates were determined (n=5

mice/genotype) (**H**). (**I**) Heart tissue sections prepared from 3-month-old *PTPMT1*$^{fl/fl}$*/MYH6-Cre*$^{+}$ and *PTPMT1*$^{+/+}$*/MYH6-Cre*$^{+}$ mice (4 mice/genotype) were processed for ROS staining. One representative picture from 4 mice/genotype is shown. (**J**) Heart tissues dissected from 6 to 8-month-old *PTPMT1*$^{fl/fl}$*/MYH6-Cre*$^{+}$ and *PTPMT1*$^{+/+}$*/MYH6-Cre*$^{+}$ mice were processed for TEM examination. One representative image from 4 mice/genotype is shown. (**K**) Heart tissue sections prepared from 10 to 12-month-old *PTPMT1*$^{fl/fl}$*/MYH6-Cre*$^{+}$ and *PTPMT1*$^{+/+}$*/MYH6-Cre*$^{+}$ mice were processed for Oil Red O staining to visualize lipids. One representative picture from 3 mice/genotype is shown.

Figure 1

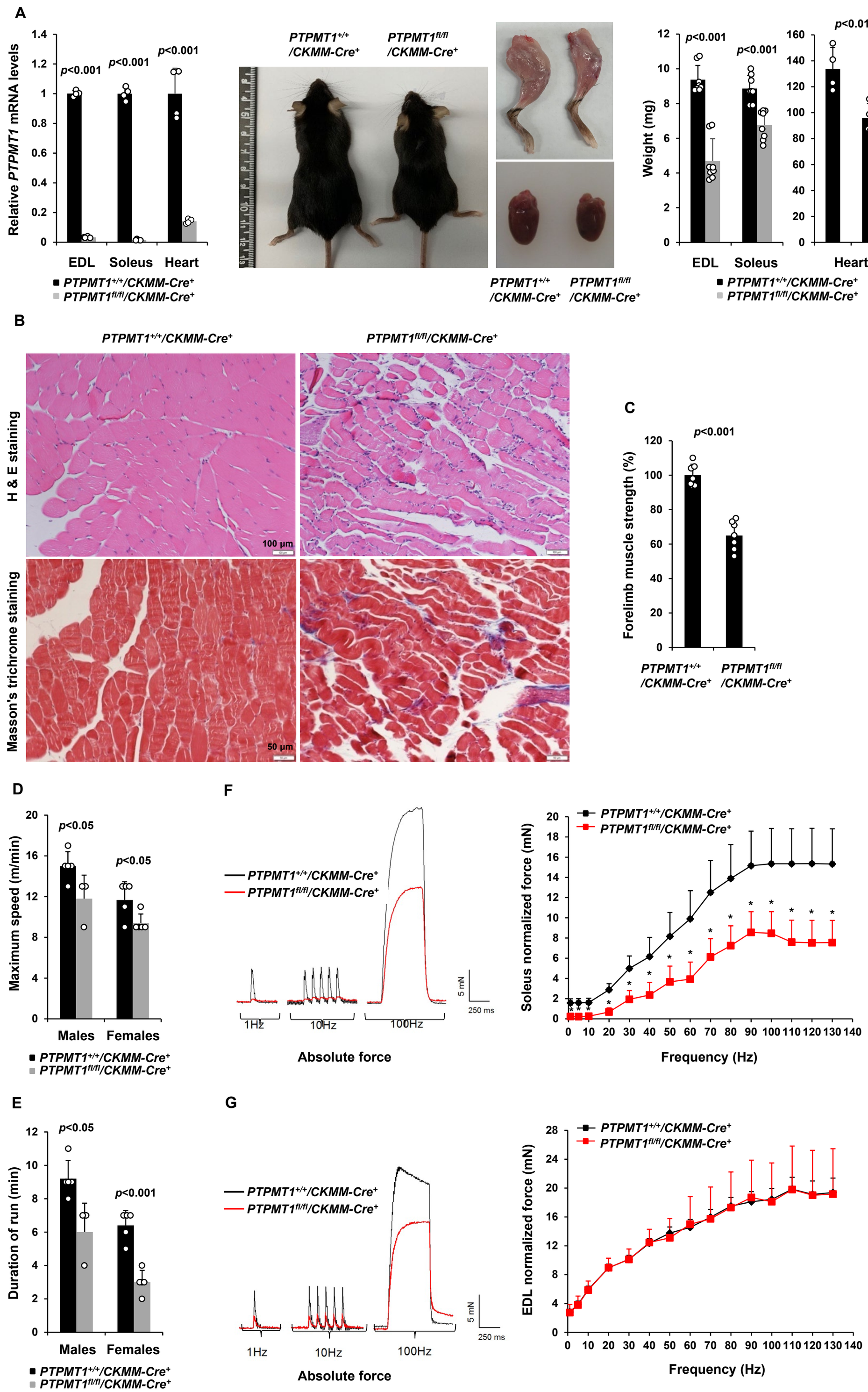
A
Relative PTPMT1 mRNA levels
p<0.001
p<0.001
p<0.001
EDL
Soleus
Heart
PTPMT1+/+/CKMM-Cre+
PTPMT1fl/fl/CKMM-Cre+
PTPMT1+/+ /CKMM-Cre+
PTPMT1fl/fl /CKMM-Cre+
Weight (mg)
p<0.001
p<0.001
p<0.01
B
H & E staining
Masson's trichrome staining
100 µm
50 µm
C
Forelimb muscle strength (%)
p<0.001
D
Maximum speed (m/min)
p<0.05
p<0.05
Males
Females
F
Absolute force
1Hz
10Hz
100Hz
5 mN
250 ms
Soleus normalized force (mN)
Frequency (Hz)
E
Duration of run (min)
p<0.05
p<0.001
G
EDL normalized force (mN)

Figure 2

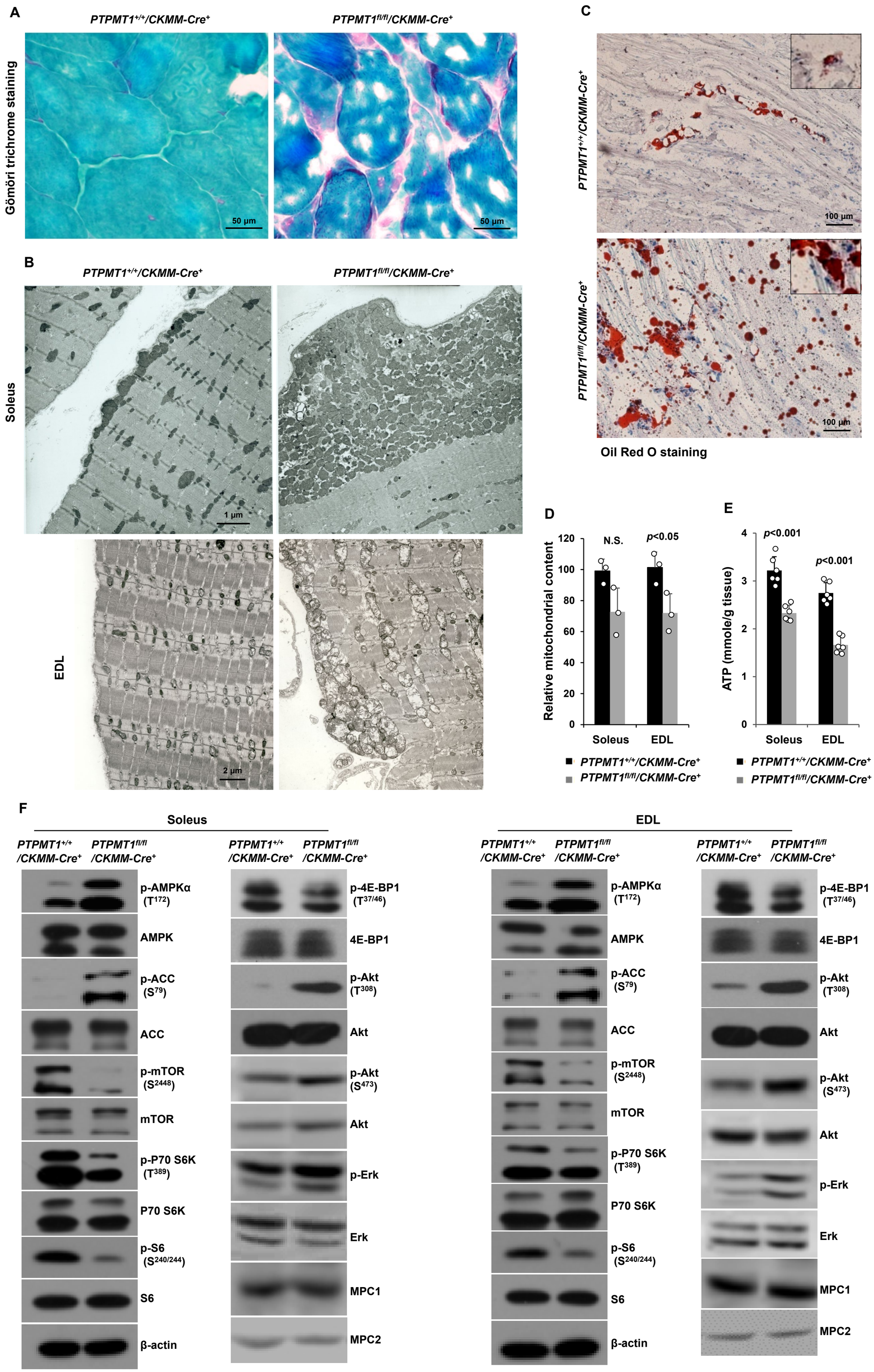
A
PTPMT1+/+/CKMM-Cre+
PTPMT1fl/fl/CKMM-Cre+
Gömöri trichrome staining
50 µm
50 µm
B
PTPMT1+/+/CKMM-Cre+
PTPMT1fl/fl/CKMM-Cre+
Soleus
1 µm
EDL
2 µm
C
PTPMT1+/+/CKMM-Cre+
PTPMT1fl/fl/CKMM-Cre+
100 µm
100 µm
Oil Red O staining
D
Relative mitochondrial content
N.S.
p<0.05
Soleus
EDL
PTPMT1+/+/CKMM-Cre+
PTPMT1fl/fl/CKMM-Cre+
E
ATP (mmole/g tissue)
p<0.001
p<0.001
Soleus
EDL
PTPMT1+/+/CKMM-Cre+
PTPMT1fl/fl/CKMM-Cre+
F
Soleus
EDL
PTPMT1+/+ /CKMM-Cre+
PTPMT1fl/fl /CKMM-Cre+
p-AMPKα (T172)
AMPK
p-ACC (S79)
ACC
p-mTOR (S2448)
mTOR
p-P70 S6K (T389)
P70 S6K
p-S6 (S240/244)
S6
β-actin
p-4E-BP1 (T37/46)
4E-BP1
p-Akt (T308)
Akt
p-Akt (S473)
Akt
p-Erk
Erk
MPC1
MPC2

Figure 3

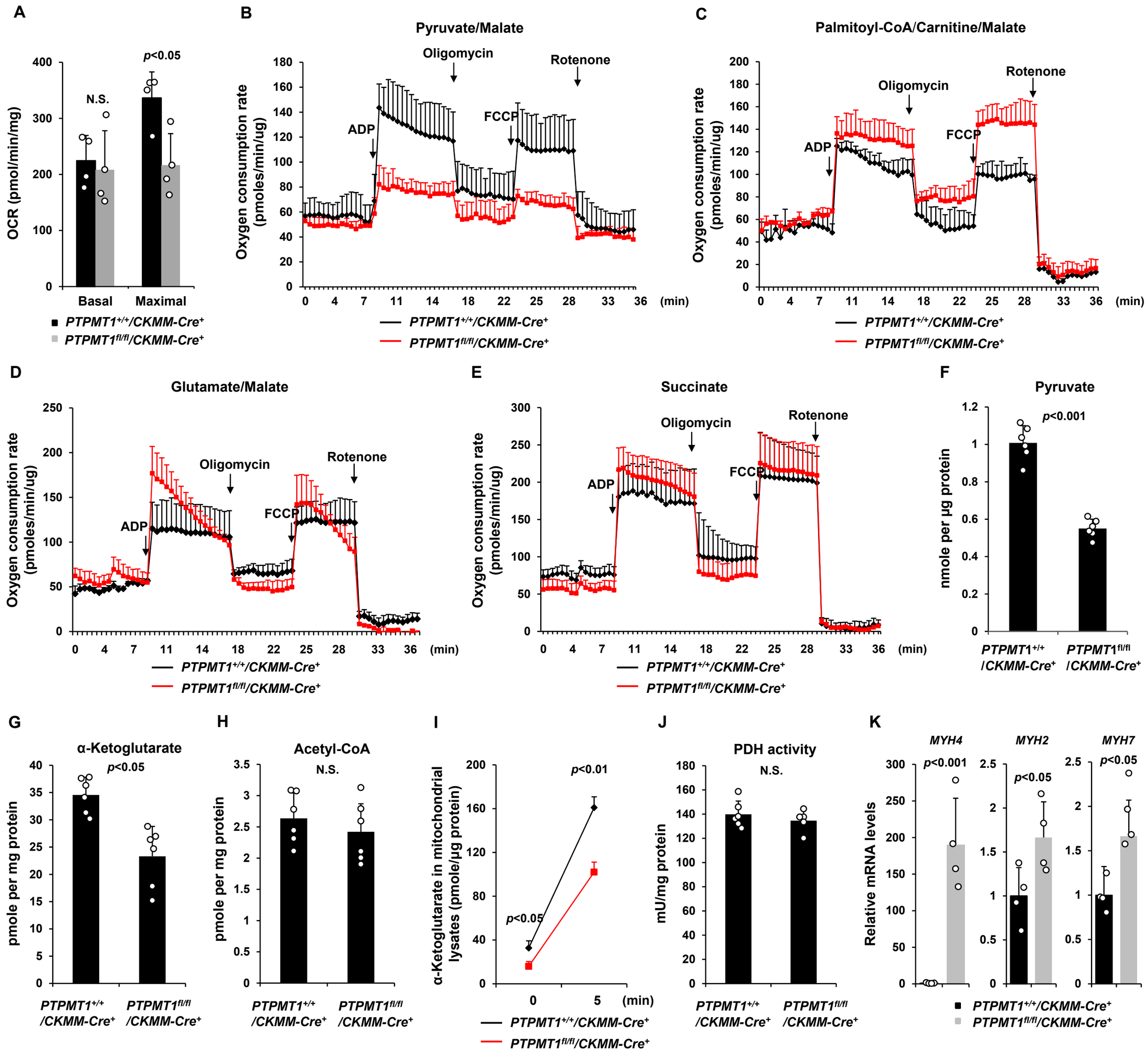
A
OCR (pmol/min/mg)
N.S.
p<0.05
Basal
Maximal
PTPMT1+/+/CKMM-Cre+
PTPMT1fl/fl/CKMM-Cre+
B
Pyruvate/Malate
Oligomycin
Rotenone
ADP
FCCP
Oxygen consumption rate (pmoles/min/ug)
(min)
C
Palmitoyl-CoA/Carnitine/Malate
D
Glutamate/Malate
E
Succinate
F
Pyruvate
p<0.001
nmole per µg protein
G
α-Ketoglutarate
p<0.05
pmole per mg protein
H
Acetyl-CoA
I
p<0.01
α-Ketoglutarate in mitochondrial lysates (pmole/µg protein)
J
PDH activity
mU/mg protein
K
MYH4
MYH2
MYH7
Relative mRNA levels

Figure 4

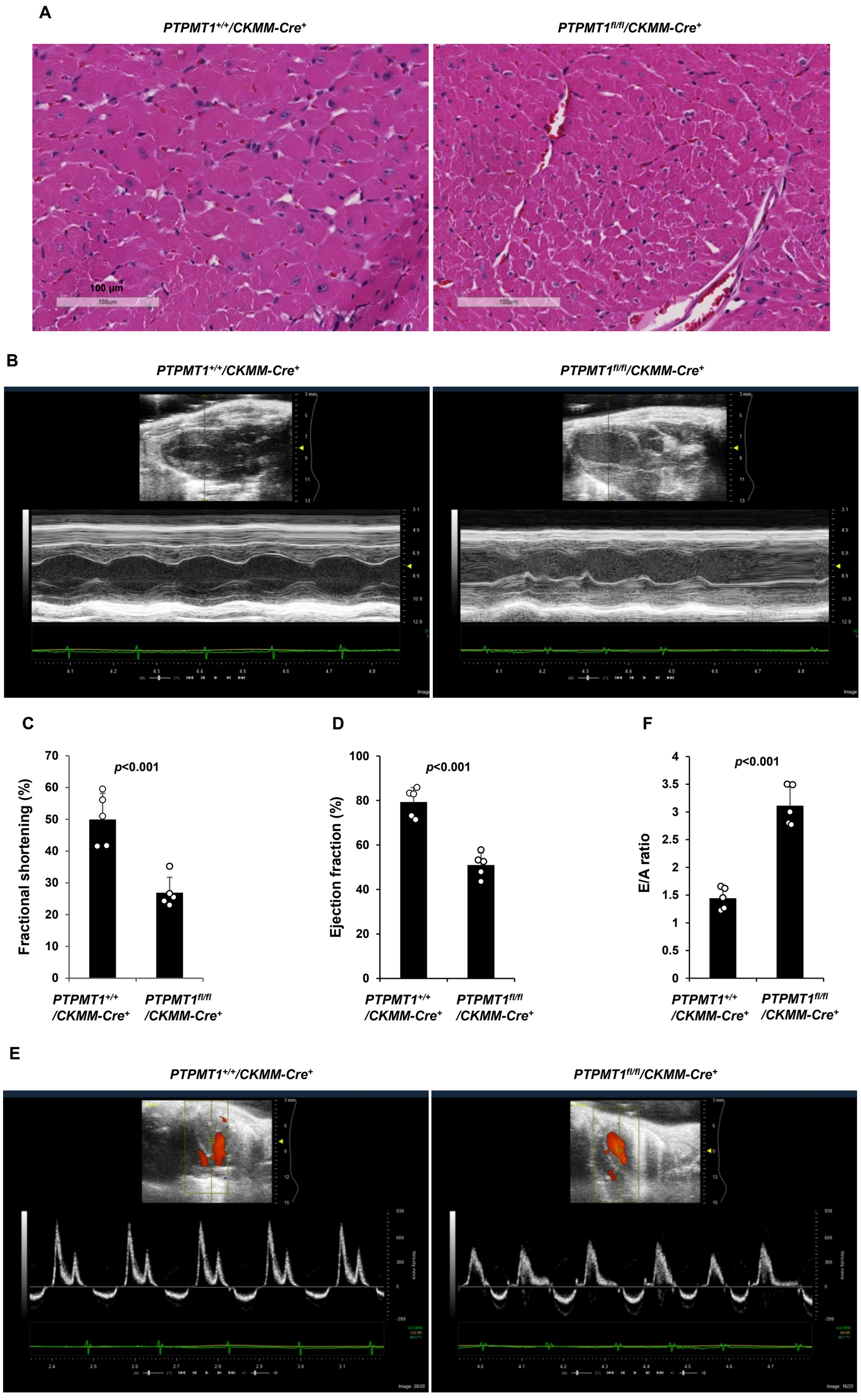
A
PTPMT1+/+/CKMM-Cre+
PTPMT1fl/fl/CKMM-Cre+
100 µm
B
PTPMT1+/+/CKMM-Cre+
PTPMT1fl/fl/CKMM-Cre+
C
Fractional shortening (%)
p<0.001
PTPMT1+/+ /CKMM-Cre+
PTPMT1fl/fl /CKMM-Cre+
D
Ejection fraction (%)
p<0.001
PTPMT1+/+ /CKMM-Cre+
PTPMT1fl/fl /CKMM-Cre+
F
E/A ratio
p<0.001
PTPMT1+/+ /CKMM-Cre+
PTPMT1fl/fl /CKMM-Cre+
E
PTPMT1+/+/CKMM-Cre+
PTPMT1fl/fl/CKMM-Cre+

Figure 5

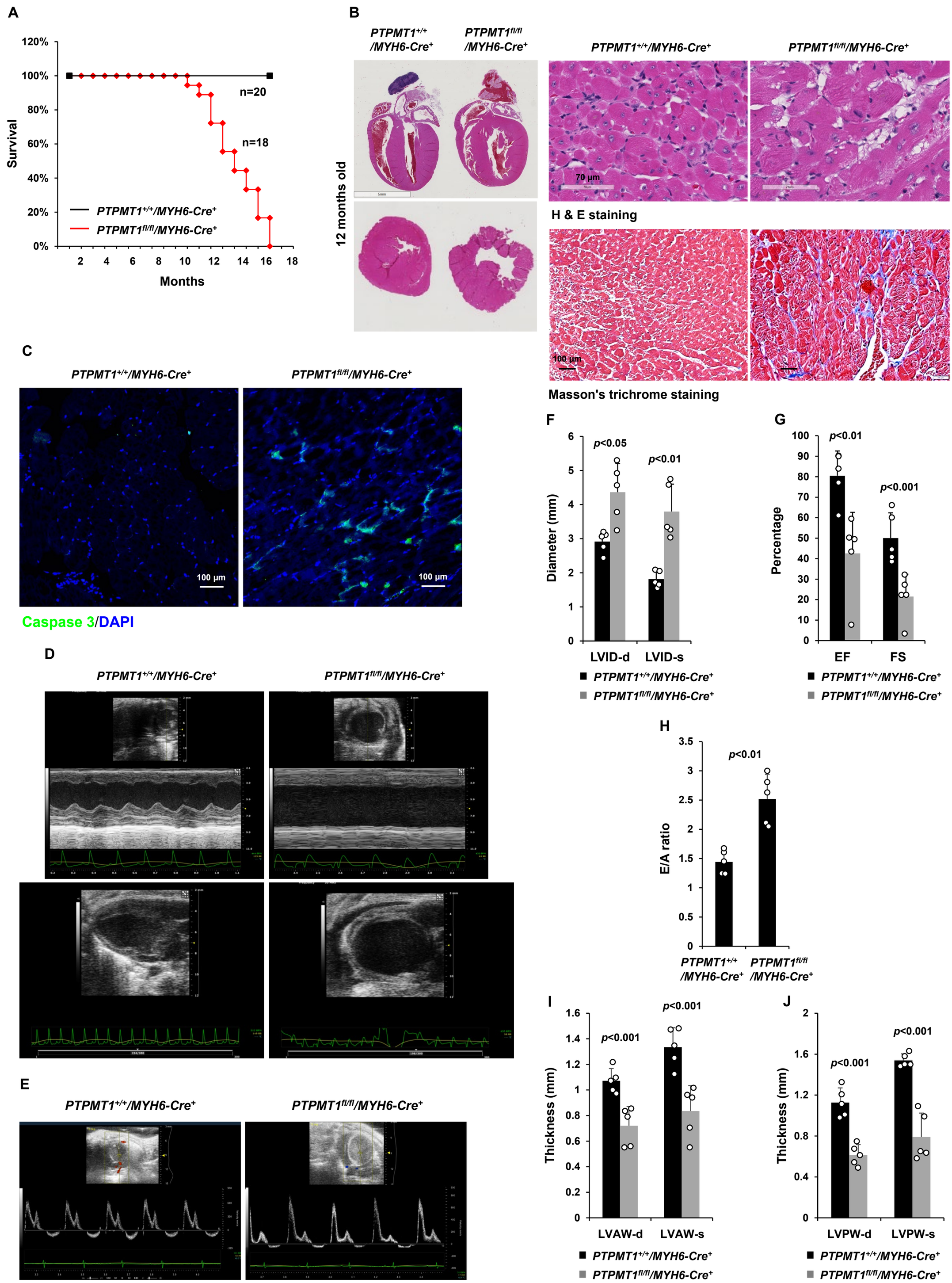
A
Survival
120%
100%
80%
60%
40%
20%
0%
n=20
n=18
PTPMT1+/+/MYH6-Cre+
PTPMT1fl/fl/MYH6-Cre+
2 4 6 8 10 12 14 16 18
Months
B
PTPMT1+/+ /MYH6-Cre+
PTPMT1fl/fl /MYH6-Cre+
12 months old
PTPMT1+/+/MYH6-Cre+
PTPMT1fl/fl/MYH6-Cre+
70 µm
H & E staining
100 µm
Masson's trichrome staining
C
PTPMT1+/+/MYH6-Cre+
PTPMT1fl/fl/MYH6-Cre+
100 µm
100 µm
Caspase 3/DAPI
D
PTPMT1+/+/MYH6-Cre+
PTPMT1fl/fl/MYH6-Cre+
E
PTPMT1+/+/MYH6-Cre+
PTPMT1fl/fl/MYH6-Cre+
F
Diameter (mm)
p<0.05
p<0.01
LVID-d LVID-s
PTPMT1+/+/MYH6-Cre+
PTPMT1fl/fl/MYH6-Cre+
G
Percentage
p<0.01
p<0.001
EF FS
PTPMT1+/+/MYH6-Cre+
PTPMT1fl/fl/MYH6-Cre+
H
E/A ratio
p<0.01
PTPMT1+/+ /MYH6-Cre+
PTPMT1fl/fl /MYH6-Cre+
I
Thickness (mm)
p<0.001
p<0.001
LVAW-d LVAW-s
PTPMT1+/+/MYH6-Cre+
PTPMT1fl/fl/MYH6-Cre+
J
Thickness (mm)
p<0.001
p<0.001
LVPW-d LVPW-s
PTPMT1+/+/MYH6-Cre+
PTPMT1fl/fl/MYH6-Cre+

Figure 6

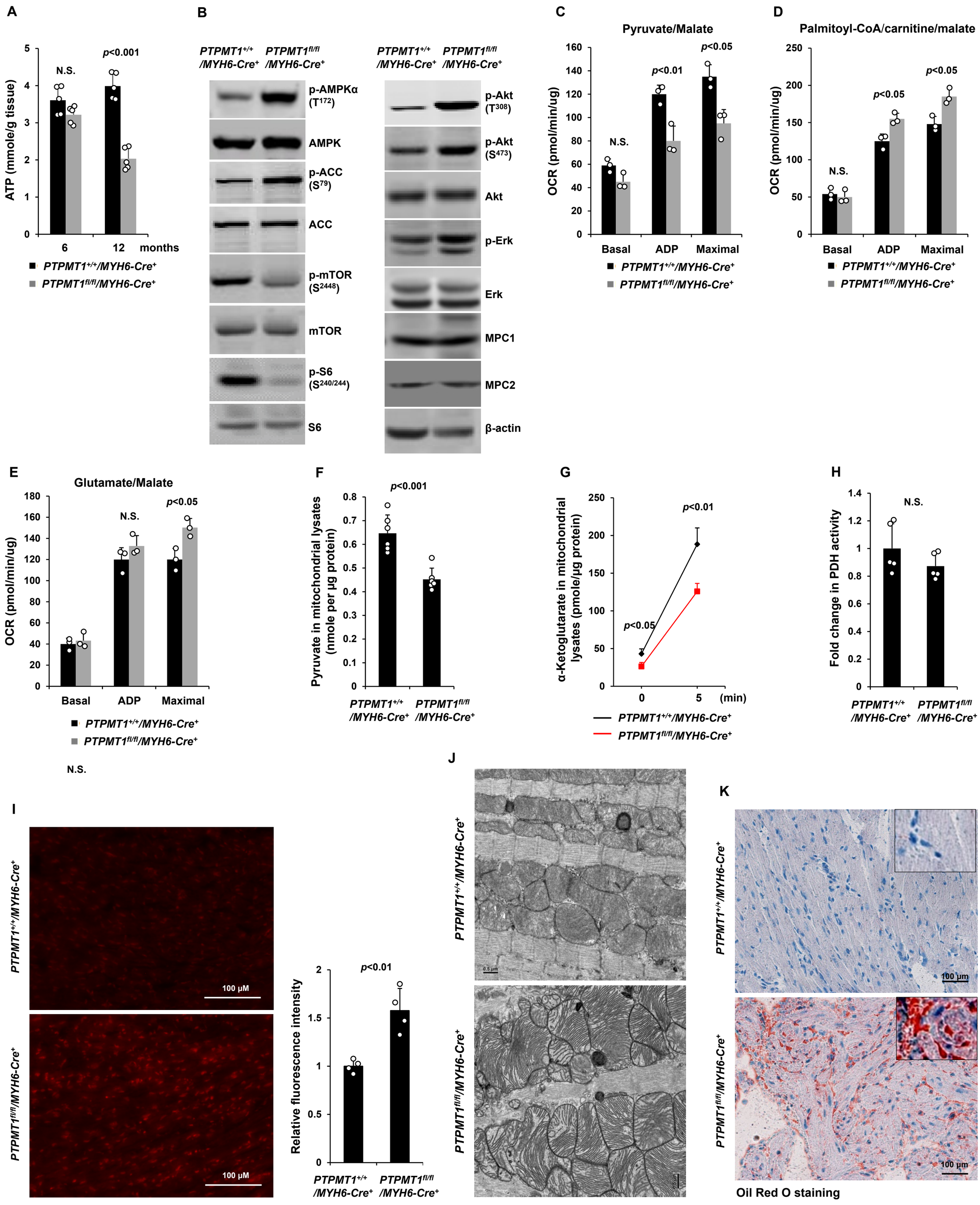
A
ATP (mmole/g tissue)
N.S.
p<0.001
6
12
months
PTPMT1+/+/MYH6-Cre+
PTPMT1fl/fl/MYH6-Cre+
B
PTPMT1+/+ /MYH6-Cre+
PTPMT1fl/fl /MYH6-Cre+
p-AMPKα (T172)
AMPK
p-ACC (S79)
ACC
p-mTOR (S2448)
mTOR
p-S6 (S240/244)
S6
p-Akt (T308)
p-Akt (S473)
Akt
p-Erk
Erk
MPC1
MPC2
β-actin
C
Pyruvate/Malate
OCR (pmol/min/ug)
N.S.
p<0.01
p<0.05
Basal
ADP
Maximal
PTPMT1+/+/MYH6-Cre+
PTPMT1fl/fl/MYH6-Cre+
D
Palmitoyl-CoA/carnitine/malate
OCR (pmol/min/ug)
N.S.
p<0.05
p<0.05
Basal
ADP
Maximal
PTPMT1+/+/MYH6-Cre+
PTPMT1fl/fl/MYH6-Cre+
E
Glutamate/Malate
OCR (pmol/min/ug)
N.S.
p<0.05
Basal
ADP
Maximal
PTPMT1+/+/MYH6-Cre+
PTPMT1fl/fl/MYH6-Cre+
N.S.
F
Pyruvate in mitochondrial lysates (nmole per µg protein)
p<0.001
PTPMT1+/+ /MYH6-Cre+
PTPMT1fl/fl /MYH6-Cre+
G
α-Ketoglutarate in mitochondrial lysates (pmole/µg protein)
p<0.01
p<0.05
0
5
(min)
PTPMT1+/+/MYH6-Cre+
PTPMT1fl/fl/MYH6-Cre+
H
Fold change in PDH activity
N.S.
PTPMT1+/+ /MYH6-Cre+
PTPMT1fl/fl /MYH6-Cre+
I
PTPMT1+/+/MYH6-Cre+
PTPMT1fl/fl/MYH6-Cre+
100 µM
100 µM
Relative fluorescence intensity
p<0.01
PTPMT1+/+ /MYH6-Cre+
PTPMT1fl/fl /MYH6-Cre+
J
PTPMT1+/+/MYH6-Cre+
PTPMT1fl/fl/MYH6-Cre+
K
PTPMT1+/+/MYH6-Cre+
PTPMT1fl/fl/MYH6-Cre+
100 µm
100 µm
Oil Red O staining